Available online at www.sciencedirect.com
SCIENCE DIRECT®
Journal of Sound and Vibration 265 (2003) 863–885
JOURNAL OF SOUND AND VIBRATION
www.elsevier.com/locate/jsvi

Effects of internal viscous damping on the stability of a rotating shaft driven through a universal joint ☆

A.J. Mazzei[a,*], R.A. Scott[b]

[a] *Department of Mechanical Engineering, Kettering University, 1-709, 1700 West Third Avenue, Flint, MI 48504-4898, USA*

[b] *Department of Mechanical Engineering, The University of Michigan, G044 W. E. Lay Automotive Laboratory, 1231 Beal Avenue, Ann Arbor, MI 48109-2121, USA*

Received 16 April 2002; accepted 18 August 2002

Abstract

A rotating flexible shaft, with both external and internal viscous damping, driven through a universal joint is considered. The mathematical model consists of a set of coupled, linear partial differential equations with time-dependent coefficients. Use of Galerkin's technique leads to a set of coupled linear differential equations with time-dependent coefficients. Using these differential equations some effects of internal viscous damping on parametric and flutter instability zones are investigated by the monodromy matrix technique. The flutter zones are also obtained on discarding the time-dependent coefficients in the differential equations which leads to an eigenvalue analysis. A one-term Galerkin approximation aided this analysis. Two different shafts ("automotive" and "lab") were considered. Increasing internal damping is always stabilizing as regards to parametric instabilities. For flutter type instabilities it was found that increasing internal damping is always stabilizing for rotational speeds v below the first critical speed, v_1. For $v > v_1$, there is a value of the internal viscous damping coefficient, C_{iv}, which depends on the rotational speed and torque, above which destabilization occurs.

The value of C_{iv} ("critical value") at which the unstable zone first enters the practical range of operation was determined. The dependence of C_{iv} critical on the external damping was investigated. It was found for the automotive case that a four-fold increase in external damping led to an increase of about 20% of the critical value. For the lab model an increase of two orders of magnitude of the external damping led to an increase of critical value of only 10%.

For the automotive shaft it was found that this critical value also removed the parametric instabilities out of the practical range. For the lab model it is not always possible to completely stabilize the system by

☆ A preliminary version of this paper was presented at the International Modal Analysis Conference XX (Los Angeles, CA, 2002) and is published in the proceedings of that conference.

*Corresponding author. Tel.: +810-762-7878; fax: 810-762-7860.

E-mail address: amazzei@kettering.edu (A.J. Mazzei).

0022-460X/03/$ - see front matter
doi:10.1016/S0022-460X(02)01256-7

increasing the internal damping. For this model using C_{iv} critical, parametric instabilities are still found in the practical range of operation.

1. Introduction

In Mazzei et al. [1], external viscous damping was included in a model of a rotating flexible shaft driven through a universal joint. In the current work internal viscous damping, which may be destabilizing depending on the rotational speed (see, for example, Refs. [2,3]), is included in the model. It is assumed that the motor is such that the driving shaft rotates at a constant speed. Internal damping may be caused by material damping such as in the model given by, for example, Ehrich [4]. As noted by Kliem et al. [5], for example, internal damping can also be due to friction. To focus solely on the effects of material damping, friction is not considered in the current work. The current model is patterned after work in Refs. [2,3,6–8], in which external and internal damping are introduced via coefficients C_{ext} and C_{iv}; external damping is proportional to the particle velocity in an inertial co-ordinate system and internal damping is proportional to the particle velocity in a rotating co-ordinate system. The mathematical model consists of a set of coupled, linear partial differential equations with time-dependent coefficients. Use of Galerkin's technique leads to a set of coupled linear differential equations with time-dependent coefficients. Using these differential equations some effects of internal viscous damping on parametric and flutter instability zones are investigated using the monodromy matrix technique. The flutter zones are also obtained on discarding the time-dependent coefficients in the differential equations which leads to an eigenvalue analysis.

2. Equations of motion

Shown in Fig. 1 is a shaft BC (length l) driven through a universal joint by a shaft AB which is rotating at a constant angular velocity Ω about its z-axis. (xyz is an inertial set of axes.) (Note that in this model the dimensions of the joint are neglected.)

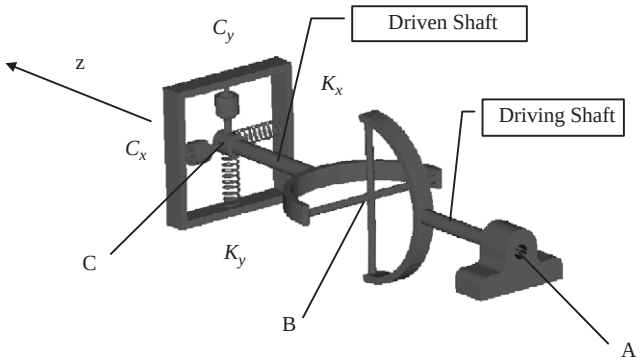

Fig. 1. Universal joint system.

External viscous damping (taken as being due to the end mount) and internal viscous damping are included. For the case of initial angles between the driving and driven shafts equal to zero,[1] the equations of motion for the driven shaft are (in non-dimensional form)

$$X_2\frac{\partial^4 U}{\partial Z^4}+v^2\frac{\partial^2 U}{\partial \tau^2}+d_1 v\frac{\partial U}{\partial \tau}\bigg|_{z=1}\Lambda(Z-1)+\underline{d_3 v\left(\frac{\partial U}{\partial \tau}+V\right)}+\Gamma_1 p_4(\tau)\frac{\mathrm{d}(\Lambda(Z))}{\mathrm{d}Z}+\Gamma_1\frac{\partial^3 V}{\partial Z^3}$$
$$=X_3 v^2\frac{\partial^4 U}{\partial Z^2\,\partial \tau^2}+X_4 v^2\frac{\partial^3 V}{\partial Z^2\,\partial \tau},$$
$$X_2\frac{\partial^4 V}{\partial Z^4}+v^2\frac{\partial^2 V}{\partial \tau^2}+d_2 v\frac{\partial V}{\partial \tau}\bigg|_{z=1}\Lambda(Z-1)+\underline{d_3 v\left(\frac{\partial V}{\partial \tau}-U\right)}-\Gamma_1 p_3(\tau)\frac{\mathrm{d}(\Lambda(Z))}{\mathrm{d}Z}-\Gamma_1\frac{\partial^3 U}{\partial Z^3}$$
$$=X_3 v^2\frac{\partial^4 V}{\partial Z^2\,\partial \tau^2}-X_4 v^2\frac{\partial^3 U}{\partial Z^2\,\partial \tau}. \tag{1}$$

The equations of motion were developed with respect to the inertial frame xyz, with the z-axis directed along the driven shaft axis and origin at the center of the universal joint (details are given in Ref. [1]).

The underscored terms represent the new additional internal damping terms. The notation is as follows: v is a non-dimensional rotation defined as $v=\Omega/\Omega_0$. Ω_0 is a reference frequency given by: $\Omega_0=(\pi^2/l^2)\sqrt{EI/\rho A}$ (the lowest bending frequency of a non-rotating pinned-pinned Euler–Bernoulli beam).

$$\Gamma_1=\frac{T_0}{\rho A\Omega_0^2 l^3},\quad X_2=\frac{EI}{\rho A\Omega_0^2 l^4},\quad X_3=\frac{R_0^2}{4l^2},\quad X_4=2X_3.$$
$$d_1=\frac{C_x}{\rho A\Omega_0 l},\quad d_2=\frac{C_y}{\rho A\Omega_0 l},\quad d_3=\frac{C_{iv}}{\rho A\Omega_0}.$$
$$p_3(\tau)=-\frac{1}{2}\left(\frac{\partial U}{\partial Z}\bigg|_{Z=0}(1+\cos 2\tau)+\frac{\partial V}{\partial Z}\bigg|_{Z=0}\sin 2\tau\right).$$
$$p_4(\tau)=-\frac{1}{2}\left(\frac{\partial V}{\partial Z}\bigg|_{Z=0}(1-\cos 2\tau)+\frac{\partial U}{\partial Z}\bigg|_{Z=0}\sin 2\tau\right).$$

$U=u/l$, $V=v/l$ are dimensionless elastic transverse deformations of the shaft neutral axis measured with respect to xyz and $Z=z/l$. $\Lambda(Z)=l\Delta(z)$, where Δ stands for the Dirac delta function. E denotes Young's modulus, I the area moment of inertia, ρ the mass density and A the cross-sectional area. τ denotes non-dimensional time ($\tau=\Omega t$). C_x and C_y are damping coefficients associated with the dashpots shown in Fig. 1 (K_x and K_y are springs rates). T_0 is the torque applied to the driving shaft AB. C_{iv} is the internal damping coefficient per unit length.

3. Galerkin's method

Eq. (1) constitute a set of coupled homogeneous partial differential equations with time-dependent coefficients. The spatial dependence in the equations is satisfied by using Galerkin's

[1] Non-zero initial angles lead to forced motion problems, items that are not of interest in the current work.

method. The solutions are assumed to have the form

$$U = \sum_{i=1}^{\infty} \Phi_i(Z) F_i(\tau), \quad V = \sum_{i=1}^{\infty} \Psi_i(Z) G_i(\tau), \tag{2}$$

where $\Phi_i(Z)$ and $\Psi_i(Z)$ are Galerkin comparison functions. For this problem they are chosen to be mode shapes of a non-rotating Euler–Bernoulli beam pinned at one end and spring supported at the other end. These functions for the xz and yz planes are, respectively,

$$\Phi_i(Z) = \sinh(H_{(x)i}Z) + \frac{\sinh(H_{(x)i})}{\sin(H_{(x)i})}\sin(H_{(x)i}Z),$$
$$\Psi_i(Z) = \sinh(H_{(y)i}Z) + \frac{\sinh(H_{(y)i})}{\sin(H_{(y)i})}\sin(H_{(y)i}Z),$$

where $H_{(x)i}$ and $H_{(y)i}$ are the positive solutions of the transcendental equation

$$H^3[\tan(H) - \tanh(H)] - 2\frac{KL^3}{EI}\tanh(H)\tan(H) = 0$$

for $K = K_x$ and $K = K_y$, respectively.

Application of the method leads to (the coefficients used in the following equations are listed in Appendix A)

$$\begin{aligned}
&v^2\begin{bmatrix} \lfloor \gamma_{1_{mi}} \rfloor - X_3\lfloor \lambda_{1_{mi}} \rfloor & [0] \\ [0] & \lfloor \gamma_{2_{mi}} \rfloor - X_3\lfloor \lambda_{2_{mi}} \rfloor \end{bmatrix}\begin{Bmatrix} \{\ddot{F}_i\} \\ \{\ddot{G}_i\} \end{Bmatrix} \\
&+ v\begin{bmatrix} d_1\lfloor \xi_{1_{mi}} \rfloor + d_3\lfloor \gamma_{1_{mi}} \rfloor & -vX_4\lfloor \lambda_{3_{mi}} \rfloor \\ vX_4\lfloor \lambda_{4_{mi}} \rfloor & d_2\lfloor \xi_{2_{mi}} \rfloor + d_3\lfloor \gamma_{2_{mi}} \rfloor \end{bmatrix}\begin{Bmatrix} \{\dot{F}_i\} \\ \{\dot{G}_i\} \end{Bmatrix} \\
&+ \begin{bmatrix} X_2\lfloor \alpha_{1_{mi}} \rfloor & d_3v\lfloor \gamma_{3_{mi}} \rfloor \\ -d_3v\lfloor \gamma_{4_{mi}} \rfloor & X_2\lfloor \alpha_{2_{mi}} \rfloor \end{bmatrix}\begin{Bmatrix} \{F_i\} \\ \{G_i\} \end{Bmatrix} \\
&+ \Gamma_1\begin{bmatrix} [0] & \lfloor \delta_{3_{mi}} \rfloor + \lfloor \beta_{1_{mi}} \rfloor \\ -\lfloor \delta_{2_{mi}} \rfloor - \lfloor \beta_{2_{mi}} \rfloor & [0] \end{bmatrix}\begin{Bmatrix} \{F_i\} \\ \{G_i\} \end{Bmatrix} \\
&+ \Gamma_1\sin(2\tau)\begin{bmatrix} \lfloor \delta_{1_{mi}} \rfloor & [0] \\ [0] & -\lfloor \delta_{4_{mi}} \rfloor \end{bmatrix}\begin{Bmatrix} \{F_i\} \\ \{G_i\} \end{Bmatrix} \\
&+ \Gamma_1\cos(2\tau)\begin{bmatrix} [0] & -\lfloor \delta_{3_{mi}} \rfloor \\ -\lfloor \delta_{2_{mi}} \rfloor & [0] \end{bmatrix}\begin{Bmatrix} \{F_i\} \\ \{G_i\} \end{Bmatrix} = \begin{Bmatrix} \{0\} \\ \{0\} \end{Bmatrix}, \\
&\quad i = 1, 2, 3, \ldots, \infty; \quad m = 1, 2, 3 \ldots, \infty.
\end{aligned} \tag{3}$$

On truncation at $i = m = N$ terms, Eqs. (3) constitute a set of $2N$ coupled differential equations with time-dependent coefficients and various skew symmetric matrices. Thus the system is prone to parametric and flutter type instabilities. It was found that the parametric instability leads to

parametric resonances of the first and second kind and the flutter instability to self-excited vibration. The instability zones can be obtained numerically by using the monodromy matrix technique (see Ref. [9]). For all the cases investigated here the monodromy procedure converged with the use of three Galerkin comparison functions. Results are presented for two distinct sets of numerical parameters, namely, for a hollow shaft of automotive proportions and for a laboratory model (a solid shaft). The parameter values for the automotive shaft are: $l = 8.96 \times 10^{-1}$, $\rho = 7.83 \times 10^{3}\,\mathrm{kg/m^3}$, $E = 2.07 \times 10^{11}\,\mathrm{N/m^2}$, $R_o = 3.4950 \times 10^{-2}\,\mathrm{m}$, $R_i = 3.3300 \times 10^{-2}\,\mathrm{m}$ (outer and inner radius, respectively), $K_x = 2.50 \times 10^{3}\,\mathrm{N/m}$, $K_y = 1.06 \times 10^{4}\,\mathrm{N/m}$, $C_{ext} = C_x = C_y = 5.0 \times 10^{-1}\,\mathrm{N/(m/s)}$. The laboratory model has the same material properties as the automotive shaft plus the following different parameters: $l = 4.6 \times 10^{-1}\,\mathrm{m}$, $R_o = 2.40 \times 10^{-3}\,\mathrm{m}$ (solid shaft), $K_x = 25.17\,\mathrm{N/m}$, $K_y = 7.74\,\mathrm{N/m}$, $C_x = C_y = 1.0 \times 10^{-3}\,\mathrm{N/(m/s)}$. Hereafter the models will be referred to as "automotive" and "lab" models, respectively.

An issue is how "reasonable" are the numerical values assigned to the damping coefficients. Following Kim et al. [7], this issue is addressed here by means of a simple model. By using a one-term Galerkin approximation in Eqs. (3), neglecting time-dependent coefficients, ignoring coupling and noting that $\tau = \Omega t$, the following set of equations can be obtained

$$F_1'' + \frac{d_1\xi_1 + d_3\gamma_1}{\gamma_1 - X_3\lambda_1}\Omega_0 F_1' + \frac{X_2\alpha_1}{\gamma_1 - X_3\lambda_1}\Omega_0^2 F_1 = 0,$$
$$G_1'' + \frac{d_2\xi_2 + d_3\gamma_2}{\gamma_2 - X_3\lambda_2}\Omega_0 G_1' + \frac{X_2\alpha_2}{\gamma_2 - X_3\lambda_2}\Omega_0^2 G_1 = 0, \tag{4}$$

where primes denote differentiation with respect to time t and the Galerkin coefficients, $\xi_1, \xi_2, \gamma_1, \gamma_2, \lambda_1, \lambda_2, \alpha_1$ and α_2 can be obtained from Appendix A by setting $m = i = 1$ in the expressions. Eqs. (4) resemble a set of simple mass–damper–spring oscillator equations and thus the damping ratios can be expressed as

$$\zeta_1 = \frac{1}{2v_1}\left(\frac{d_1\xi_1 + d_3\gamma_1}{\gamma_1 - X_3\lambda_1}\right), \quad \zeta_2 = \frac{1}{2v_2}\left(\frac{d_2\xi_2 + d_3\gamma_2}{\gamma_2 - X_3\lambda_2}\right), \tag{5}$$

where $v_1 = \Omega_1/\Omega_0$ and $v_2 = \Omega_2/\Omega_0$ are the first two critical speeds of the shaft. Note that ζ_1 refers to motions on the xz plane while ζ_2 refers to motions on the yz plane.

In order to assess the accuracy of the one-term approximation, some simulations were conducted using a three-term Galerkin approximation. The stable response of the system of equations to a specified set of initial conditions was obtained for the three-term approximation and the damping ratios were evaluated based on a logarithmic decrement procedure. It was found that the one-term approximation usually underestimates the amount of damping when compared to the results obtained from the three-term approximation, but the values are quite close (within 10% for all the parameters tested). For instance, when using an internal damping coefficient $C_{iv} = 5.0\,\mathrm{N\,s/m}$, and external damping coefficients $C_{ext} = 0.5\,\mathrm{N\,s/m}$, the one-term approach leads to $\zeta_1 = 0.0239$ and $\zeta_2 = 0.0117$ whereas the logarithmic decrement procedure gives $\zeta_1 = 0.0245$ and $\zeta_2 = 0.0123$. These results lend confidence of the reasonableness of the one-term approach in estimating damping ratios in the system.

Eqs. (5) include the effect of both external and internal damping and will be used throughout this work as an approximation for the overall damping ratios of the system described by Eqs. (3).

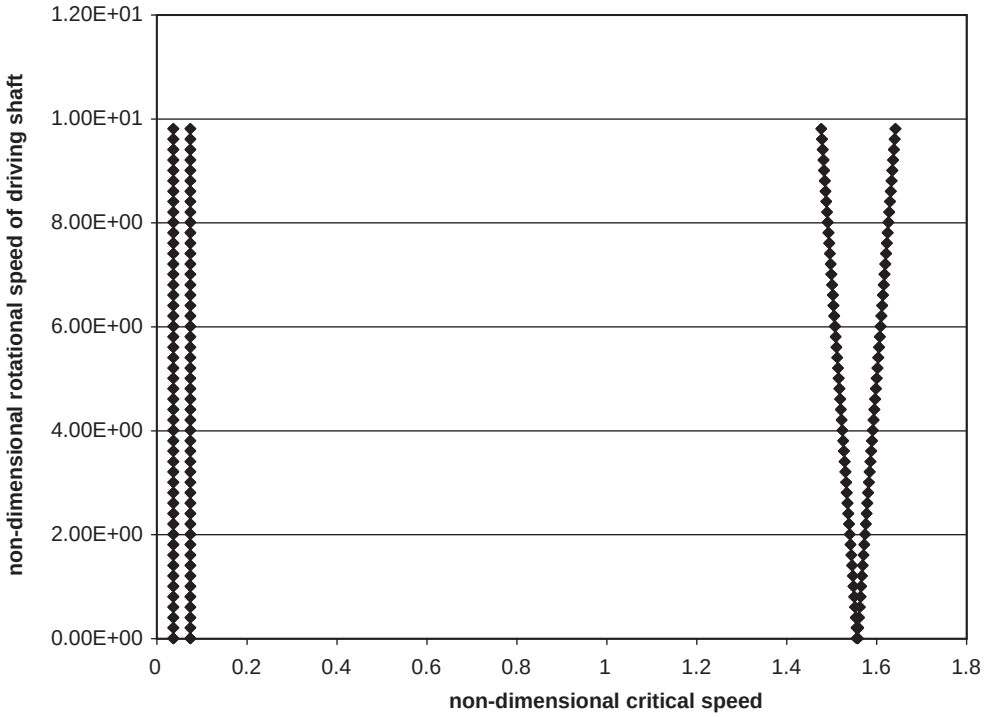

Fig. 2. Campbell diagram for automotive shaft.

Eqs. (5) can then be applied to both examples cited above and for zero internal damping the damping ratios obtained are: (1) automotive: $\zeta_1 = 0.0055$, $\zeta_2 = 0.0026$; (2) lab: $\zeta_1 = 0.0012$, $\zeta_2 = 0.0007$. It is seen that external damping is very light for both models.

Instability regions are sought in the parameter space Γ_1 (dimensionless driving torque) versus v (dimensionless driving rotation). In assessing the regions, it is useful to know the values of the critical speeds and how they depend on the rotation (so-called Campbell diagrams). A Campbell diagram can be obtained by disregarding the time-dependent coefficients in Eqs. (3), setting the driving torque to zero and solving the eigenvalue problem associated with the resulting equations for different values of driving rotation.

Fig. 2 shows the Campbell diagram for the automotive shaft. There are four critical speeds which for zero rotational speed are: $v_1 = 0.036$ (553 r.p.m.), $v_2 = 0.074$ (1077 r.p.m.), $v_3 = 1.563$ (24,000 r.p.m.), $v_4 = 1.565$ (24,040 r.p.m.). (The first set of speeds is associated with rigid motions of the shaft (shaft bouncing on springs) whereas the second set is associated with shaft flexible vibrations.) The speeds for the case involving flexibility are very high, and are outside the range of practical operation (maximum rotational speed for this case is taken to be 8000 r.p.m.). Note that there is no discernible variation in the critical speeds for the rigid case when the rotational speed is increased. Therefore, for all intents and purposes the critical speeds are the same as the natural frequencies for the non-rotating case. Similar behavior was found for the laboratory model. The first four critical speeds for this case are $v_1 = 0.067$ (180 r.p.m.), $v_2 = 0.121$ (327 r.p.m.), $v_3 = 1.564$ (4223 r.p.m.), $v_4 = 1.569$ (4236 r.p.m.).

4. Parametric instabilities

The effects of internal damping on parametric instabilities will first be discussed.

Fig. 3 shows the parametric and flutter type instabilities for the automotive system for the case where the internal damping is zero ($\zeta_1 = 0.0055$, $\zeta_2 = 0.0026$). (In Figs. 3–7, the external damping is given by $C_{ext} = 5.0 \times 10^{-1}$ N/(m/s).) They were obtained using the monodromy matrix technique (see, for example, Ref. [9]; the technique captures both parametric- and flutter-type instabilities). Zones I and II are principal zones of instability (associated with the first two critical speeds, v_1 and v_2 shown by vertical lines in the plot) while zones III and IV denote combination type instabilities (sum and difference type, respectively). These zones of instability are due to rigid body modes, i.e., the shaft bouncing on springs. For this case, zones due to shaft flexibility are outside the range in the plots.

Next the internal damping is increased to $C_{iv} = 0.5$ N s/m with the same external damping as before (overall damping ratios are $\zeta_1 = 0.0074$ and $\zeta_2 = 0.0036$). As shown in Fig. 4, this has a slight stabilizing effect on the system in that the instability boundaries are raised. For this case parametric type instabilities show a small decrease as a result of internal damping increase.

Fig. 5 shows the instabilities for the system when the internal damping is set to $C_{iv} = 5.0$ N s/m ($\zeta_1 = 0.0239$, $\zeta_2 = 0.0117$). It is seen that this value of internal damping has a more significant stabilizing effect on the parametric instabilities.

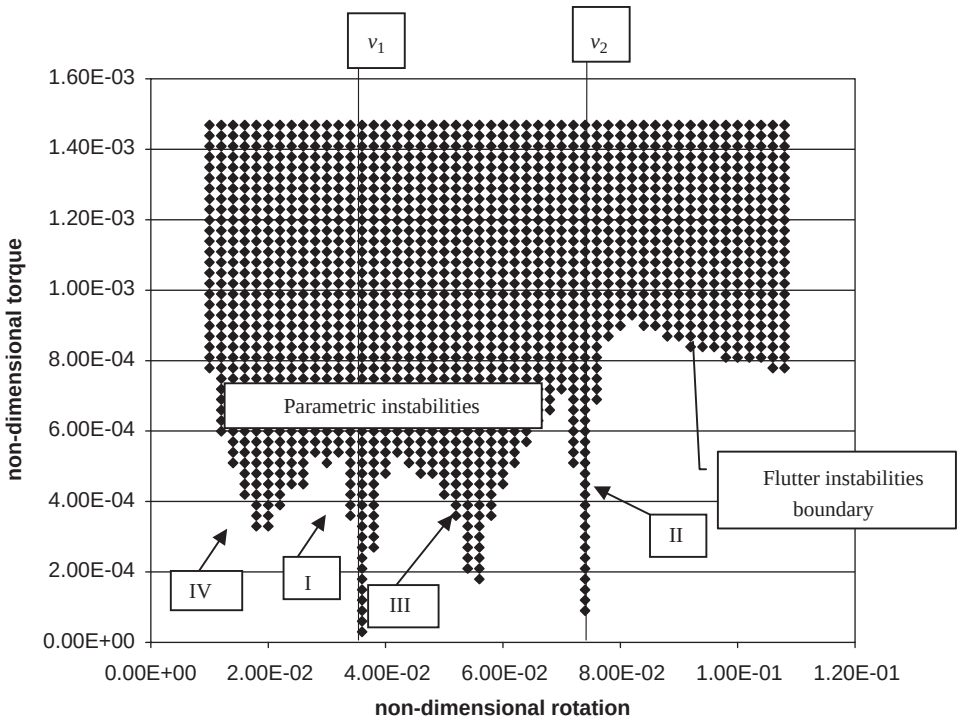

Fig. 3. Shaft instabilities for the case of zero internal damping (hashed zones indicate instability).

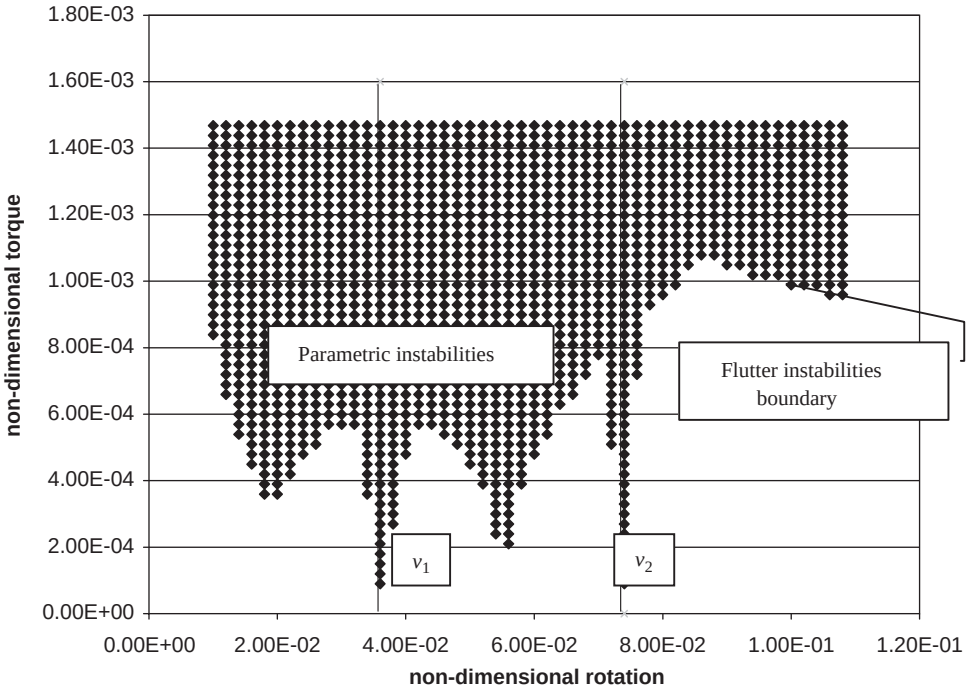

Fig. 4. Shaft instabilities for the case of internal damping = external damping (hashed zones indicate instability).

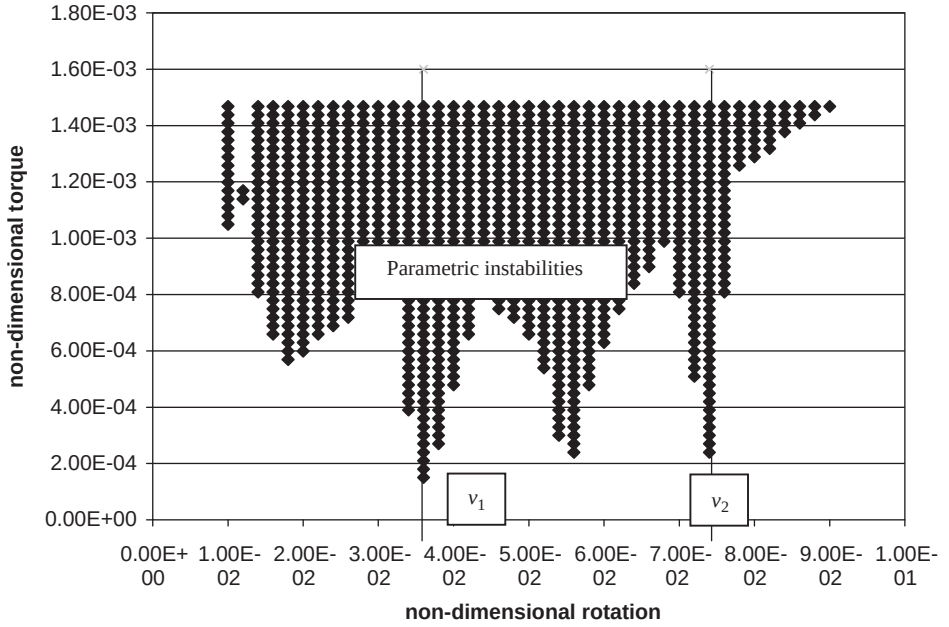

Fig. 5. Shaft instabilities for the case of internal damping an order of magnitude higher than external damping (hashed zones indicate instability).

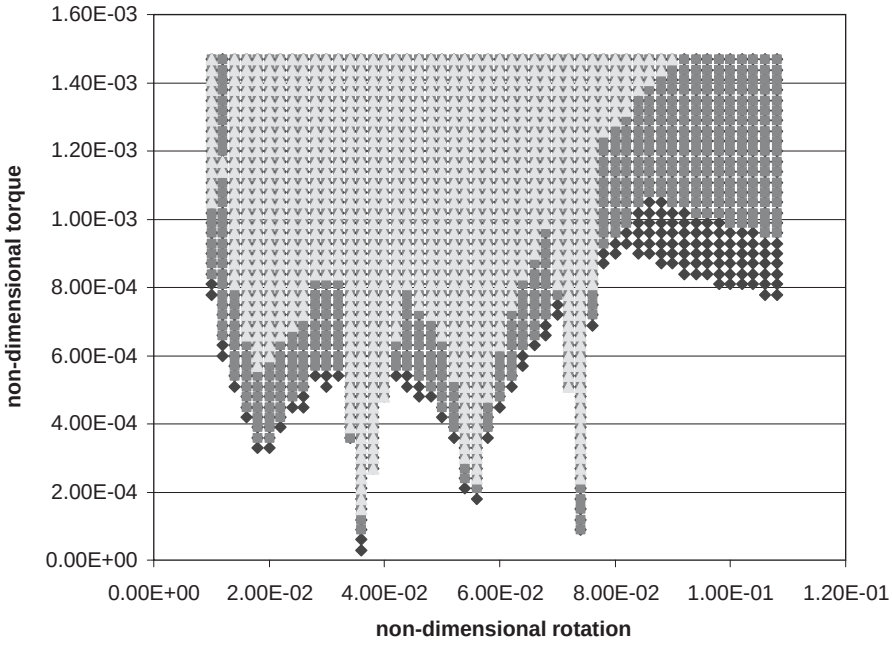

Fig. 6. Overlap of instability regions for different values of internal damping (♦, $C_{iv} = 0$; ■, $C_{iv} = 0.5$; ▲, $C_{iv} = 5.0$).

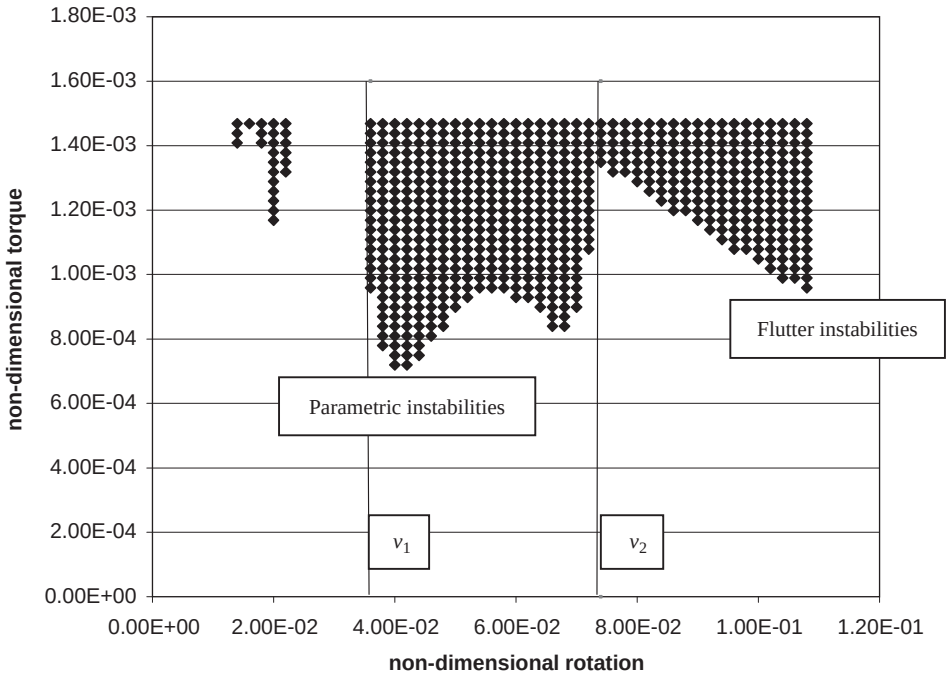

Fig. 7. Shaft instabilities for the case of internal damping two orders of magnitude higher than external damping (hashed zones indicate instability).

Fig. 6 shows an overlap for the three cases discussed above. Note the gradual stabilizing effect of the internal damping increase on the parametric instabilities.

Next, the internal damping is increased to $C_{iv} = 50\,\mathrm{N\,s/m}$ ($\zeta_1 = 0.1887$, $\zeta_2 = 0.0931$). As shown in Fig. 7 this value of damping has a considerable stabilizing effect on the system. For this case all parametric instabilities occur for a level of torque over $\Gamma_1 = 0.0005$ (corresponding to $1.7 \times 10^3\,\mathrm{N\,m}$) which is the torque that would cause static yielding of the shaft. Thus parametric instabilities are reduced to a level where they are no longer of practical importance.

Note that for small values of external damping C_{ext}, the combination zones are wider than the principal zones, but as C_{ext} increases the trend reverses (this was also noted by Mazzei et al. in Ref. [1]).

Next the lab model is examined. Fig. 8 shows the instabilities for the lab model for the case where internal damping is zero ($\zeta_1 = 0.0012$, $\zeta_2 = 0.0007$). Note that in the lab model parametric instabilities due to rigid and flexible modes occur for practical rotational speeds ($v < 2$, i.e., 5360 r.p.m.). The effect of increased internal damping is observed in Fig. 9. The figure shows an overlap of zones of instability for the following values of internal damping: $C_{iv} = 0$ ($\zeta_1 = 0.0012$, $\zeta_2 = 0.0007$), $C_{iv} = 0.001\,\mathrm{N\,s/m}$ ($\zeta_1 = 0.0016$, $\zeta_2 = 0.0009$) and $C_{iv} = 0.01\,\mathrm{N\,s/m}$ ($\zeta_1 = 0.0053$, $\zeta_2 = 0.0030$). (In Figs. 8–10 the external damping is given by $C_{ext} = 1.0 \times 10^{-3}\,\mathrm{N/(m/s)}$). Note that, as in the automotive example, parametric instabilities are reduced when internal damping increases. For the example, a value of $C_{iv} = 0.001\,\mathrm{N\,s/m}$ ($\zeta_1 = 0.0016$, $\zeta_2 = 0.0009$, same as external damping) produces a small stabilizing effect on the system, whereas a value of $C_{iv} = 0.01\,\mathrm{N\,s/m}$ ($\zeta_1 = 0.0053$, $\zeta_2 = 0.0030$, an order of magnitude higher than external damping) has a

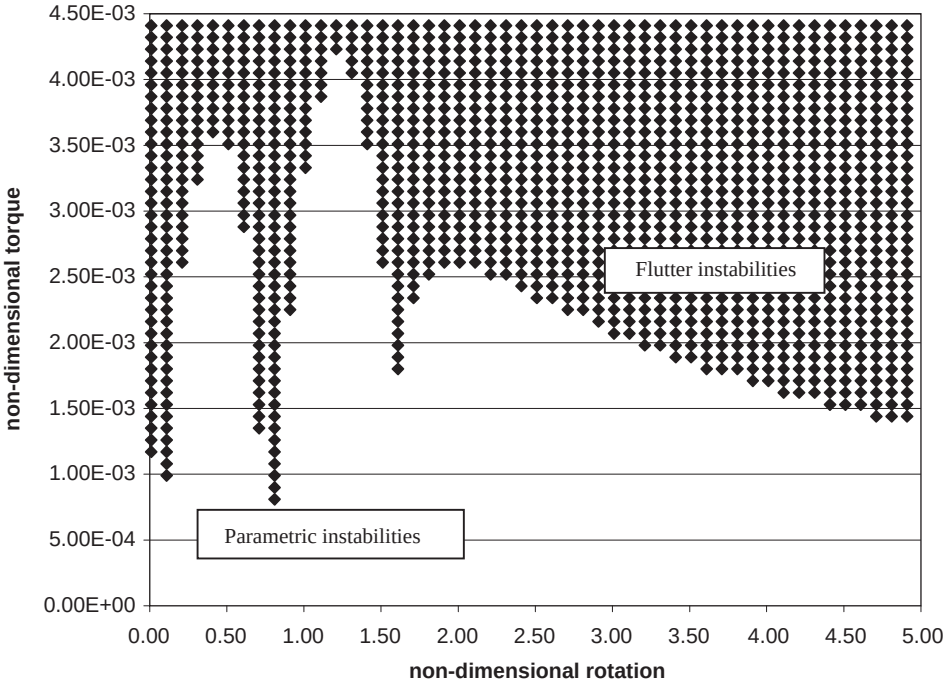

Fig. 8. Shaft instabilities for the case of zero internal damping (hashed zones indicate instability).

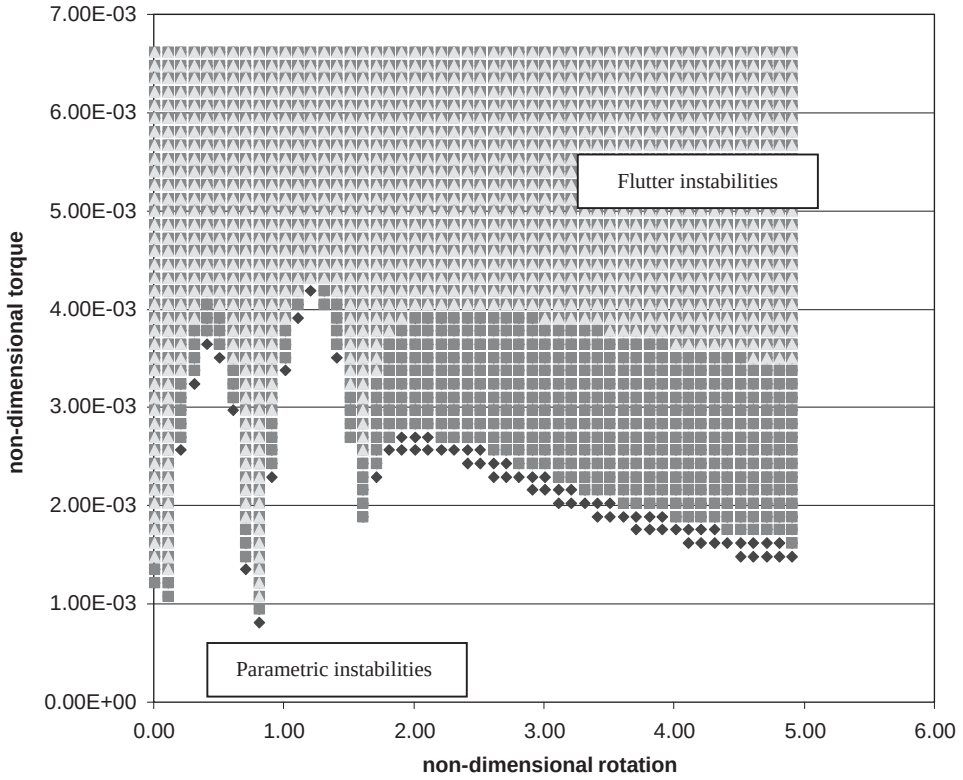

Fig. 9. Overlap of zones of instability for different values of internal damping (hashed zones indicate instability; ♦, $C_{iv} = 0$; ■, $C_{iv} = 1.00 \times 10^{-3}$; ▲, $C_{iv} = 1.00 \times 10^{-2}$).

more pronounced stabilizing effect. Fig. 10 shows the instabilities for the lab model when the internal damping has a value of $C_{iv} = 0.15\,\mathrm{N\,s/m}$ ($\zeta_1 = 0.0629$, $\zeta_2 = 0.0353$). It can be seen in the plot that when this value of damping is applied to the lab model, parametric instabilities only occur for values of torque over $\Gamma_1 = 0.0021$. This is considered to be the upper limit for operational conditions in this example[2] and, therefore, this relatively low value of internal damping can rid the system of parametric instabilities.

5. Flutter instabilities

Flutter instabilities will now be addressed. Consider first the automotive example. Shown in Fig. 11 are the flutter boundaries (as well as parametric instability zones) for $C_{iv} = 0$ ($\zeta_1 = 0.0055$, $\zeta_2 = 0.0026$), $C_{iv} = 0.5\,\mathrm{N\,s/m}$ ($\zeta_1 = 0.0074$, $\zeta_2 = 0.0036$) and $C_{iv} = 5.0\,\mathrm{N\,s/m}$ ($\zeta_1 = 0.0239$, $\zeta_2 = 0.0117$) ($C_{ext} = 5.0 \times 10^{-1}\,\mathrm{N/(m/s)}$). The stability boundaries for $C_{iv} = 0.5\,\mathrm{N\,s/m}$, and $C_{iv} = 5.0\,\mathrm{N\,s/m}$ are denoted by ABC and DE, respectively. The boundary of ABC is exponential in

[2] The yield torque for the lab shaft is $\Gamma = 0.0042$. A value of torque $\Gamma = 0.0021$ produces a static twist angle of about 10°. The latter is chosen as a practical limit for the torque in this example.

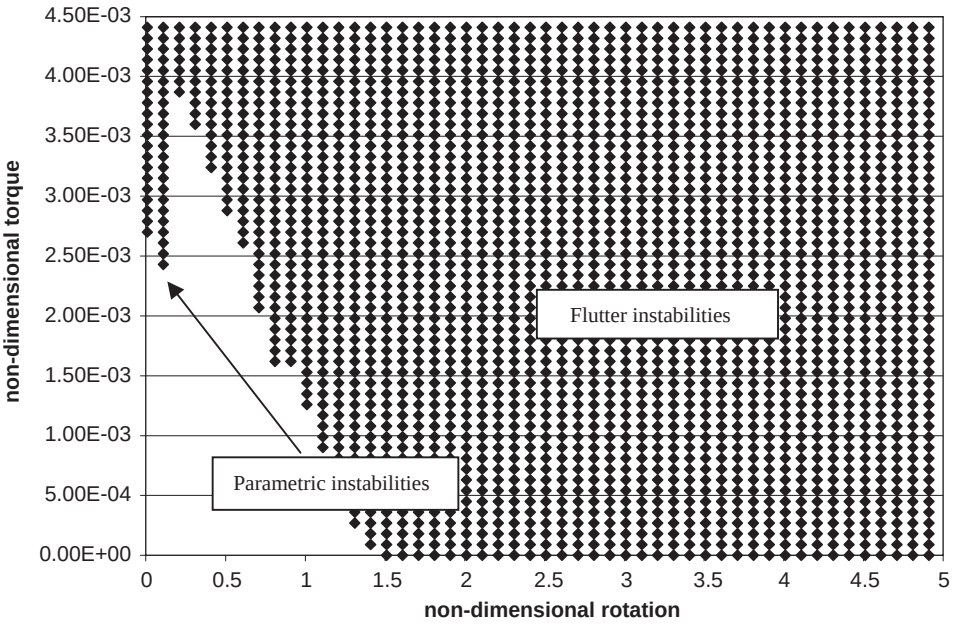

Fig. 10. Shaft instabilities for the case of internal damping $C_{iv} = 0.15\,\mathrm{N\,s/m}$ (hashed zones indicate instability).

nature and its asymptote is essentially horizontal. It is judged that the value $C_{iv} = 0.5\,\mathrm{N\,s/m}$ is always stabilizing, regardless of the magnitude of the rotational speed v. For the values of v shown in Fig. 11, $C_{iv} = 5.0\,\mathrm{N\,s/m}$ is always stabilizing. However it is conjectured that since DE shows a linear decrease (in contrast to ABC) there will be a value of v above which destabilization occurs (when DE intersects the horizontal asymptote ABC; this value is not pursued here, since it would be outside the practical range of operation). Note that it has been numerically observed that the straight-line behavior occurs when the internal damping is dominant.

In the case of the lab model similar behavior was observed. It is seen in Fig. 9 that flutter instabilities diminish for increasing values of internal damping. However, destabilization occurs when a value of $C_{iv} = 0.15\,\mathrm{N\,s/m}$ ($\zeta_1 = 0.0629$, $\zeta_2 = 0.0353$), for example, is used (compare Figs. 8–10). Here the increase of internal damping leads to an increase in the flutter instability zone. Note that for this case instabilities occur for all points in the torque–speed space that have speeds above $v = 1.5$ (approximately 4000 r.p.m.) which is below the upper speed boundary for this shaft and consequently can create unstable conditions inside the range of operation.

From the previous discussion a natural question that arises concerns the value of C_{iv} at which destabilization first occurs and its dependence on rotational speed. The monodromy matrix technique is very computationally intensive so this issue will be addressed as follows. Discarding the time-dependent coefficients in Eqs. (3) leads to the following set of equations:

$$v^2[M]\{\ddot{Q}\} + v[D]\{\dot{Q}\} + [S]\{Q\} = \{0\}, \tag{6}$$

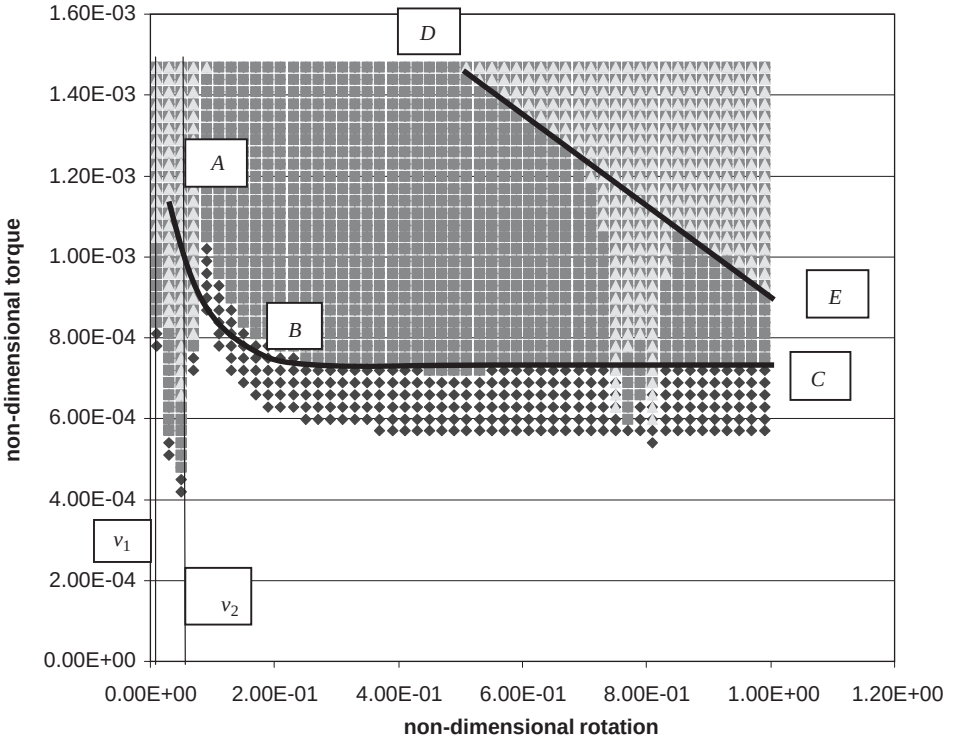

Fig. 11. Overlap of instability regions for different values of internal damping over an extended range of rotational speed (♦, $C_{iv} = 0$; ■, $C_{iv} = 0.5$; ▲, $C_{iv} = 5.0$).

where

$$[M] = \begin{bmatrix} \lfloor \gamma_{1_{mi}} \rfloor - X_3 \lfloor \lambda_{1_{mi}} \rfloor & [0] \\ [0] & \lfloor \gamma_{2_{mi}} \rfloor - X_3 \lfloor \lambda_{2_{mi}} \rfloor \end{bmatrix},$$

$$[D] = \begin{bmatrix} d_1 \lfloor \xi_{1_{mi}} \rfloor + d_3 \lfloor \gamma_{1_{mi}} \rfloor & -vX_4 \lfloor \lambda_{3_{mi}} \rfloor \\ vX_4 \lfloor \lambda_{4_{mi}} \rfloor & d_2 \lfloor \xi_{2_{mi}} \rfloor + d_3 \lfloor \gamma_{2_{mi}} \rfloor \end{bmatrix},$$

$$[S] = \begin{bmatrix} X_2 \lfloor \alpha_{1_{mi}} \rfloor & d_3 v \lfloor \gamma_{3_{mi}} \rfloor + \Gamma_1 \lfloor \delta_{3_{mi}} \rfloor + \Gamma_1 \lfloor \beta_{1_{mi}} \rfloor \\ -d_3 v \lfloor \gamma_{4_{mi}} \rfloor - \Gamma_1 \lfloor \delta_{2_{mi}} \rfloor - \Gamma_1 \lfloor \beta_{2_{mi}} \rfloor & X_2 \lfloor \alpha_{2_{mi}} \rfloor \end{bmatrix},$$

$$\{Q\} = \begin{Bmatrix} \{F_i\} \\ \{G_i\} \end{Bmatrix}.$$

Eqs. (6) predict instability whenever the associated eigenvalues have a positive real part.

In order to demonstrate accuracy of Eqs. (6) for predicting flutter type instabilities, eigenvalue extraction is used to obtain the instability zones of the automotive shaft for the following values of internal damping: $C_{iv} = 0$ ($\zeta_1 = 0.0055$, $\zeta_2 = 0.0026$), $C_{iv} = 0.5\,\mathrm{N\,s/m}$ ($\zeta_1 = 0.0074$, $\zeta_2 = 0.0036$) and $C_{iv} = 5.0\,\mathrm{N\,s/m}$ ($\zeta_1 = 0.0239$, $\zeta_2 = 0.0117$). These are shown in an overlap format in Fig. 12. Boundaries ABC and DE are also shown. Comparing these results to the ones obtained using the

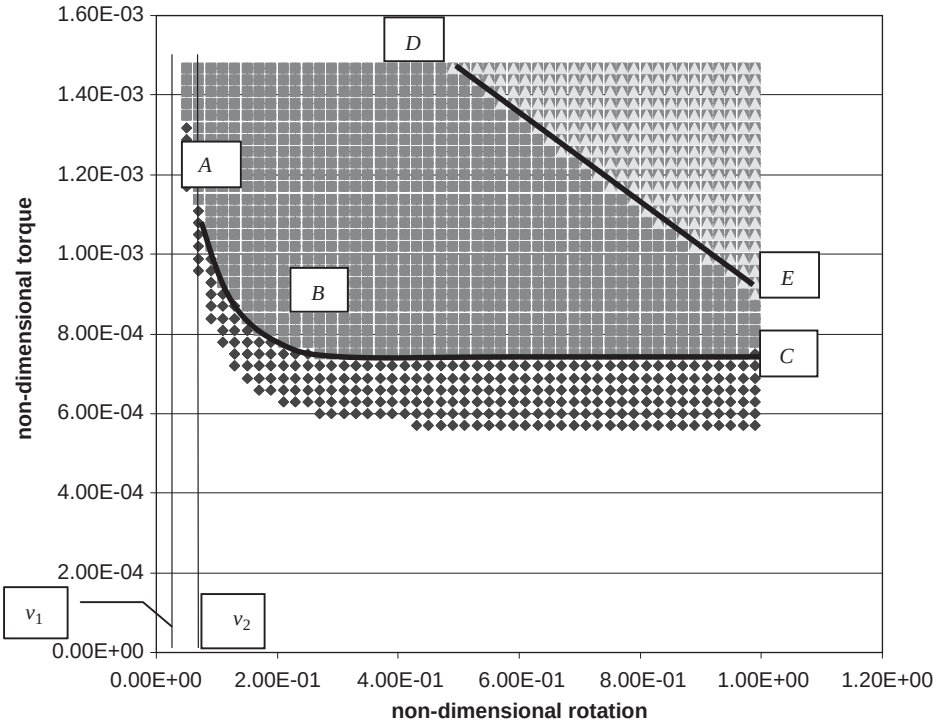

Fig. 12. Overlap of flutter instability regions for different values of internal damping (♦, $C_{iv} = 0$; ■, $C_{iv} = 0.5$; ▲, $C_{iv} = 5.0$).

monodromy matrix (see Fig. 11) excellent agreement is seen. These observations lend confidence to the eigenvalue analysis for flutter prediction and therefore this technique is used in the following discussion.

Fig. 13 shows an overlap of flutter instabilities for the automotive model when the internal damping is set to $C_{iv} = 0.5\,\mathrm{N\,s/m}$ and $C_{iv} = 50\,\mathrm{N\,s/m}$ ($\zeta_1 = 0.1887$, $\zeta_2 = 0.0931$). Consider a typical point P_1 which lies below the first critical speed. Note that for $C_{iv} = 0.5\,\mathrm{N\,s/m}$ P_1 is an unstable point. When the internal damping is increased to $C_{iv} = 50\,\mathrm{N\,s/m}$ the point becomes stable. Consider next a second typical point P_2 above the first critical speed. Note that in this case for $C_{iv} = 0.5\,\mathrm{N\,s/m}$ the point is stable while for $C_{iv} = 50\,\mathrm{N\,s/m}$ the point becomes unstable. For this case increasing the internal damping can be destabilizing.

For the lab model an overlap of flutter instability zones is shown in Fig. 14. (In both Figs. 14 and 15 external damping is given by $C_{\mathrm{ext}} = 1.0 \times 10^{-3}\,\mathrm{N/(m/s)}$.) The cases shown are: $C_{iv} = 0$ ($\zeta_1 = 0.0012$, $\zeta_2 = 0.0007$), $C_{iv} = 0.001\,\mathrm{N\,s/m}$ ($\zeta_1 = 0.0016$, $\zeta_2 = 0.0009$) and $C_{iv} = 0.01\,\mathrm{N\,s/m}$ ($\zeta_1 = 0.0053$, $\zeta_2 = 0.0030$). It is seen that flutter instabilities decrease over the range observed when internal damping is increased. (This is the same trend observed in Fig. 9 which was obtained utilizing the monodromy method.) Simulations using the eigenvalue analysis and involving still higher values of internal damping led to increased flutter instabilities for this model (as shown by the monodromy method, for example, in Fig. 10). Consider the overlap plot shown in Fig. 15. In the plot P_1 is a point that lies below the first critical speed and is stabilized by an internal damping

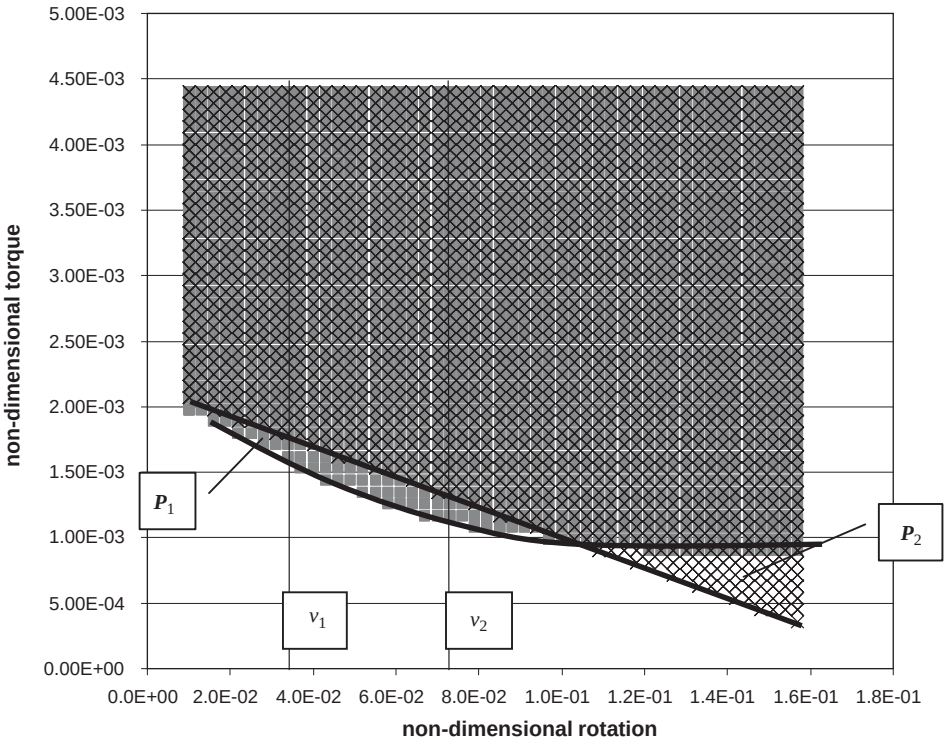

Fig. 13. Overlap of flutter regions for the automotive model (■, $C_{iv} = 0.5$; ×, $C_{iv} = 50$).

increase (from $C_{iv} = 1.50$ to 3.0 N s/m i.e., $\zeta_1 = 0.6183$, $\zeta_2 = 0.3464$ to $\zeta_1 = 1.2354$, $\zeta_2 = 0.6922$), whereas P_2 is a point above the first critical speed that is destabilized by an internal damping increase (note however that the associated ζ values are probably too high to be attainable in practice).

The data for both models shows that there is a value of C_{iv}, which depends on the rotational speed $v\cdot$ and torque Γ_1, above which destabilization occurs. For that value of C_{iv} that leads to destabilization to be of practical importance, the associated speed v and torque Γ_1 should lie in the practical range of operation. The value of C_{iv} for which the unstable zone first enters the practical range is herein called the "critical value" and this issue will be addressed in the following. (The dependency of C_{iv} on external damping will be investigated later.)

Consider first the automotive model. Fig. 16 shows the boundaries for the flutter zones of the automotive model for different values of internal damping. The lines in the plot correspond to the boundary of the flutter zones obtained via the eigenvalue analysis. The rectangular region ($0 < \Gamma_1 < 0.0004$; $0 < v < 0.4$) in the figure defines the operational range for the shaft. Note that an internal damping value of $C_{iv} = 16$ N s/m ($\zeta_1 = 0.0642$, $\zeta_2 = 0.0316$) brings the flutter boundary close to the operational range chosen. Thus this is approximately the critical value for this range, i.e., higher values of internal damping will lead to instability for operational conditions. The value of $C_{iv} = 16$ N s/m was obtained by a trial and error procedure. A more systematic approach is as follows.

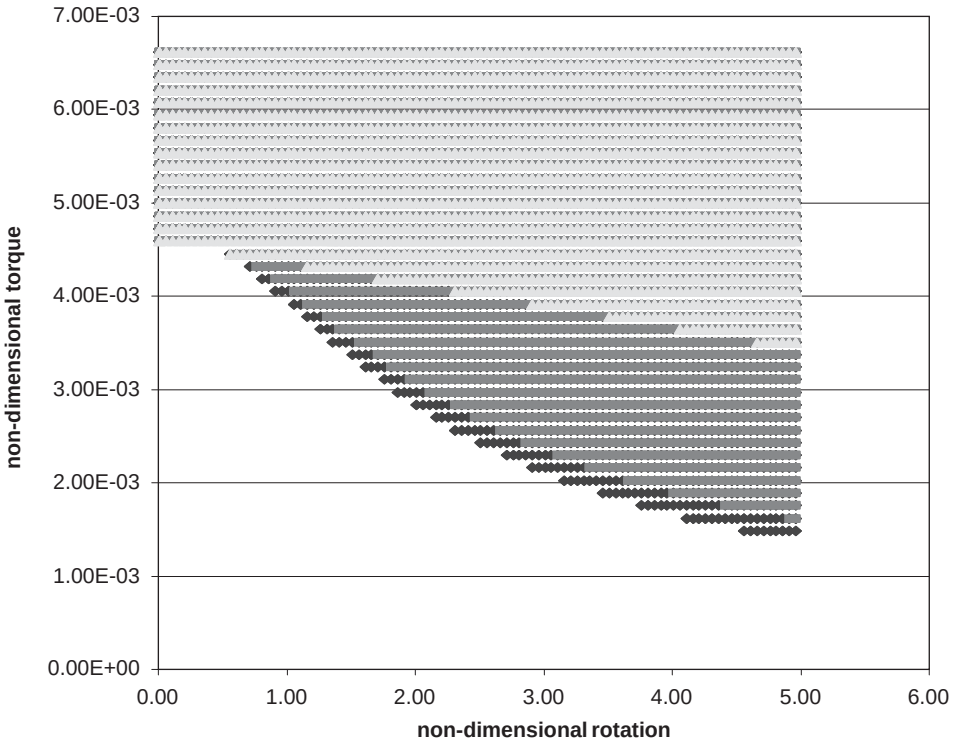

Fig. 14. Overlap of flutter instability zones for different values of internal damping (hashed zones indicate instability; ◆, $C_{iv} = 0$; ■, $C_{iv} = 1.00 \times 10^{-3}$; ▲, $C_{iv} = 1.00 \times 10^{-2}$).

A one term Galerkin approximation to Eqs. (6) leads to the matrix

$$\begin{bmatrix} \dfrac{\Omega_0(d_1\xi_1 + d_3\gamma_1)}{-\gamma_1 + X_3\lambda_1} & -\dfrac{\Omega_0 v X_4 \lambda_3}{-\gamma_1 + X_3\lambda_1} & \dfrac{\Omega_0^2 X_2 \alpha_1}{-\gamma_1 + X_3\lambda_1} & \dfrac{\Omega_0^2(d^3 v\gamma_3 + \Gamma_1\delta_3 + \Gamma_1\beta_1)}{-\gamma_1 + X_3\lambda_1} \\ \dfrac{\Omega_0 v X_4 \lambda_4}{-\gamma_2 + X_3\lambda_2} & \dfrac{\Omega_0(d_2\xi_2 + d_3\gamma_2)}{-\gamma_2 + X_3\lambda_2} & \dfrac{\Omega_0^2(-d_3 v\gamma_4 - \Gamma_1\delta_2 - \Gamma_1\beta_2)}{-\gamma_2 + X_3\lambda_2} & \dfrac{\Omega_0^2 X_2 \alpha_2}{-\gamma_2 + X_3\lambda_2} \\ 1 & 0 & 0 & 0 \\ 0 & 1 & 0 & 0 \end{bmatrix}. \quad (7)$$

The eigenvalues of matrix (7) can be expressed (using MAPLE) as functions of the internal damping and their real part can be plotted for different values of damping. This simple scheme gives an estimate of the value of C_{iv} at which flutter instabilities first enter the operational zone. Its accuracy can then be checked using the full eigenvalue analysis. (Results for the automotive shaft were also checked using a Routh–Hurwitz approach.) For the right upper corner point of the rectangular operational zone ($v = 0.4$, $\Gamma_1 = 0.0004$), the real and imaginary parts of all of the eigenvalues are plotted in Fig. 17 as functions of C_{iv}. The plot shows the eigenvalue variation for internal damping ranging from $C_{iv} = 0$ ($\zeta_1 = 0.0055$, $\zeta_2 = 0.0026$), to $C_{iv} = 20\,\mathrm{N\,s/m}$ ($\zeta_1 = 0.0788$, $\zeta_2 = 0.0388$). Note that the real parts of two of them enter the positive range and consequently cause flutter instabilities to occur.

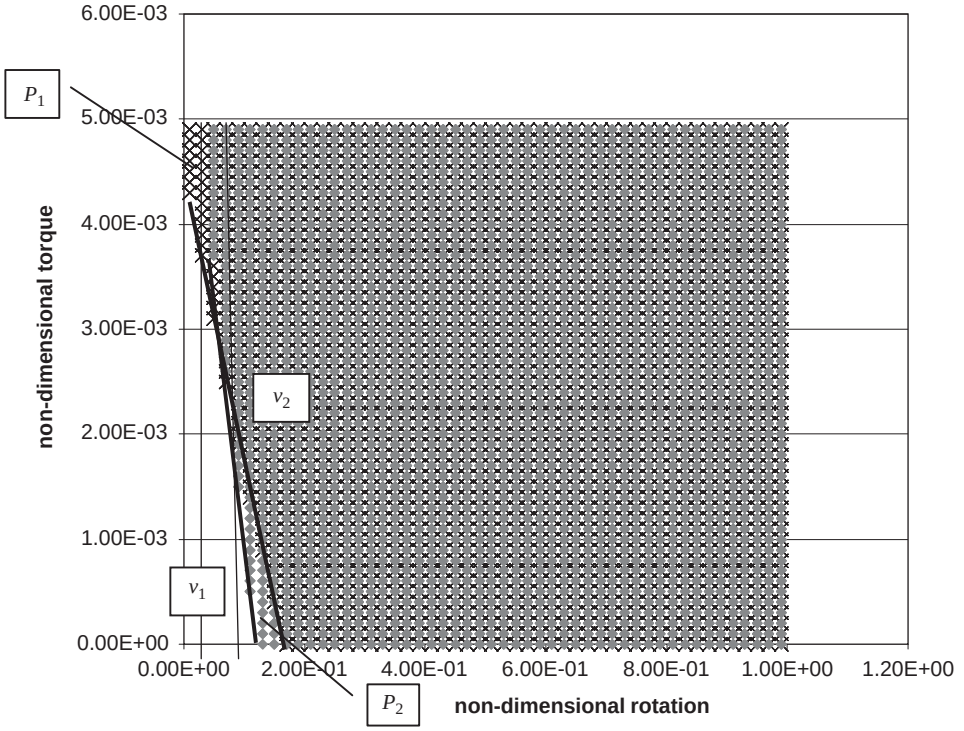

Fig. 15. Overlap of flutter instability zones for different values of internal damping (hashed zones indicate instability; ×, $C_{iv} = 1.50$; ♦, $C_{iv} = 3.00$).

In order to find the specific value of C_{iv} for which instabilities will occur a plot of one of these eigenvalues as a function of internal damping is shown in Fig. 18. Note that at $C_{iv} = 15.6\,\mathrm{N\,s/m}$ ($\zeta_1 = 0.0627$, $\zeta_2 = 0.0309$), the real part becomes positive and so instability occurs. (This value agrees well with the one obtained by using the full eigenvalue analysis seen in Fig. 16.)

Next the approximation is used to derive an estimate for a critical value for the lab model. For this example the real part becomes positive approximately for a value of $C_{iv} = 0.037\,\mathrm{N\,s/m}$ ($\zeta_1 = 0.0164$, $\zeta_2 = 0.0092$). This estimate was used in a full eigenvalue analysis and after some iterations Fig. 19 was obtained. From the figure it is judged that $C_{iv} = 0.040\mathrm{N\,s/m}$ ($\zeta_1 = 0.0177$, $\zeta_2 = 0.0099$). This result shows that the approximation also gives a good estimate of the critical value in the case of the lab model. The rectangular region defining the operational range for the model is given by $0 < \Gamma_1 < 0.0021$ and $0 < v < 2.0$.

The above data was obtained for specific values of external damping ($C_{ext} = C_x = C_y = 5.0 \times 10^{-1}$ N s/m for the automotive shaft and $C_{ext} = C_x = C_y = 1.0 \times 10^{-3}$ N s/m for the lab shaft). A natural question is how does the critical value of C_{iv} change with C_{ext}. Table 1 shows the variation of the critical damping for the automotive shaft when the overall damping ratios are increased approximately five times ($\zeta_1 = 0.06$ to $\zeta_1 = 0.29$ and $\zeta_2 = 0.03$ to $\zeta_2 = 0.14$). It is seen that the critical damping varies about 20% with external damping for the automotive shaft. Results for the lab model are shown in Table 2. It can be seen that the critical damping value is much less susceptible to increases in external damping. For this case, an increase in external

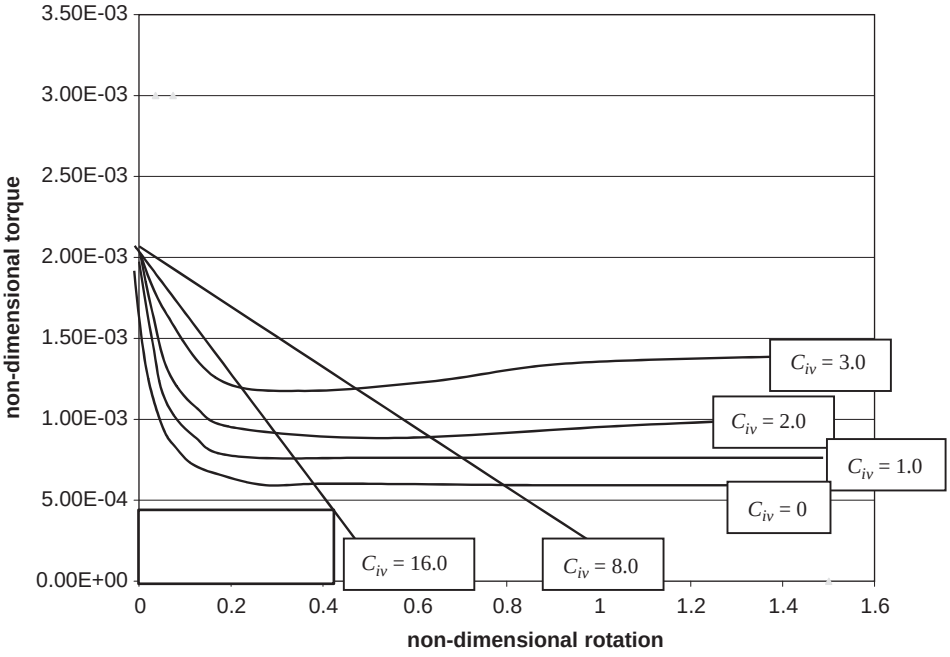

Fig. 16. Boundaries for flutter instability zones for different values of internal damping.

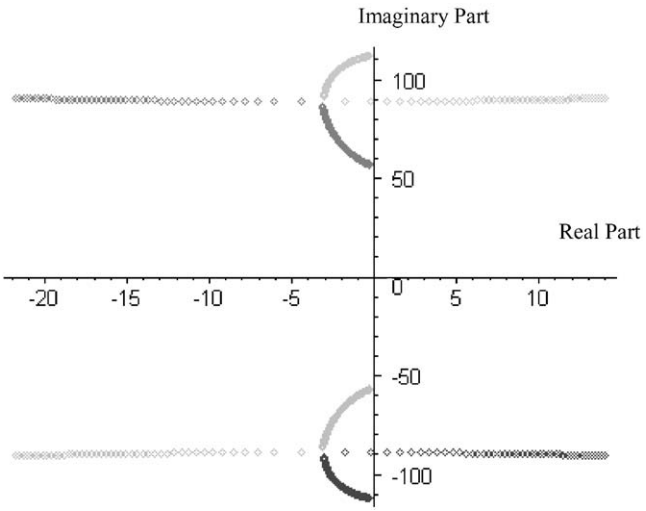

Fig. 17. Eigenvalues for the automotive example for internal damping varying from $C_{iv} = 0$; $C_{iv} = 20\,\mathrm{N\,s/m}$.

damping of two orders of magnitude led to a change in the critical value of only about 10%. These results were obtained using the approximation since it was shown that it works well for both models.

One final item that arises concerns the possible existence of a value of C_{iv} which will rid the system of parametric instabilities keeping flutter instabilities outside the range of practical

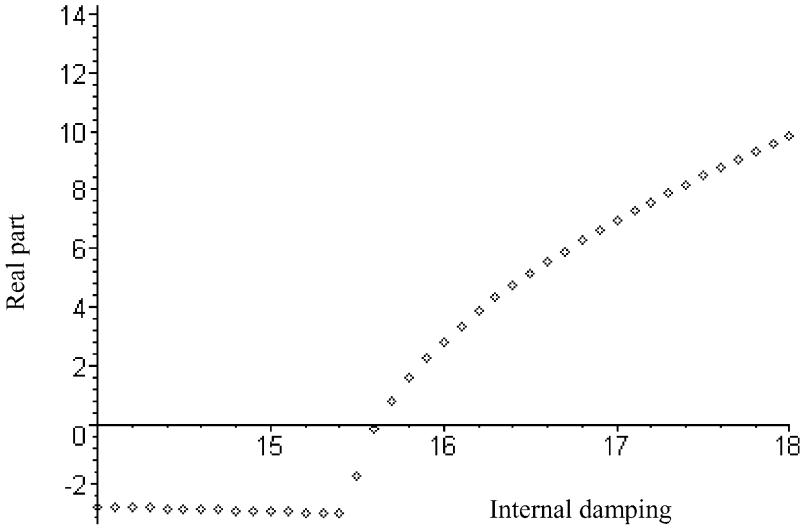

Fig. 18. Real part of one of the eigenvalues for the automotive example as a function of internal damping.

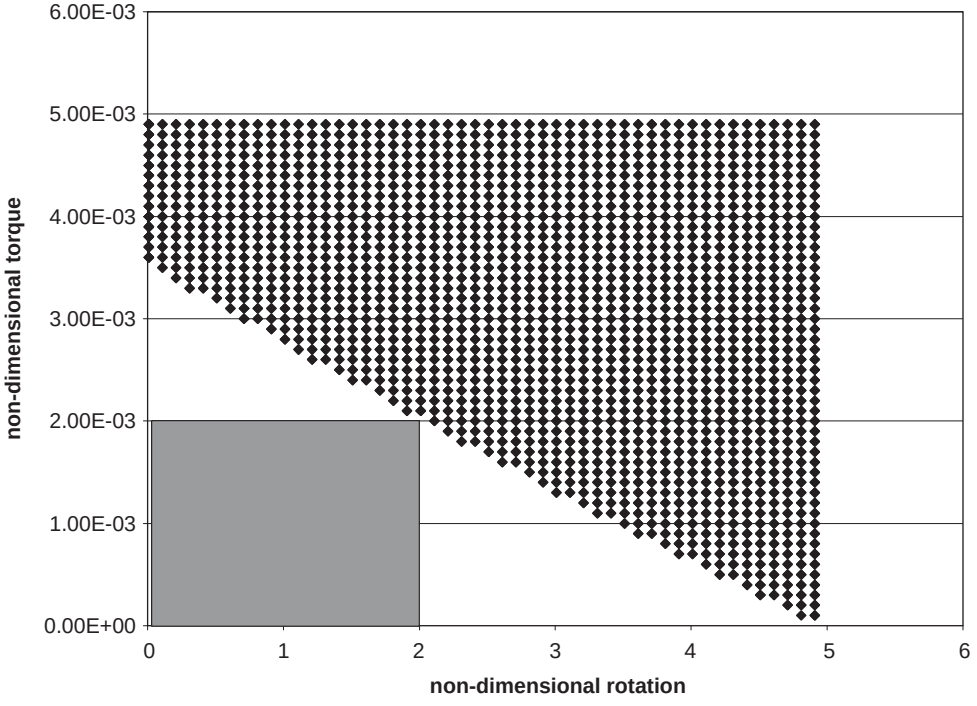

Fig. 19. Flutter Instabilities for the lab model for $C_{iv} = 0.040\,\mathrm{N\,s/m}$.

operation. Consider the automotive model. Table 1 shows that the lowest value of C_{iv} is 15.5 N s/m. Fig. 20 shows the instability regions for the automotive model for this value obtained using the monodromy matrix technique. It is seen that both parametric and flutter instabilities

Table 1
Critical damping as a function of external damping—automotive shaft

C_{crit}	C_{ext}	ς_1	ς_2
15.5	0	0.06	0.03
16.0	5.0	0.11	0.06
16.5	10.0	0.17	0.08
17.5	15.0	0.23	0.11
18.5	20.0	0.29	0.14

Table 2
Critical damping as a function of external damping—lab shaft

C_{crit}	C_{ext}	ς_1	ς_2
0.037	0	0.0152	0.0085
0.038	0.001	0.0170	0.0094
0.040	0.080	0.1133	0.0635
0.042	0.100	0.1382	0.0775

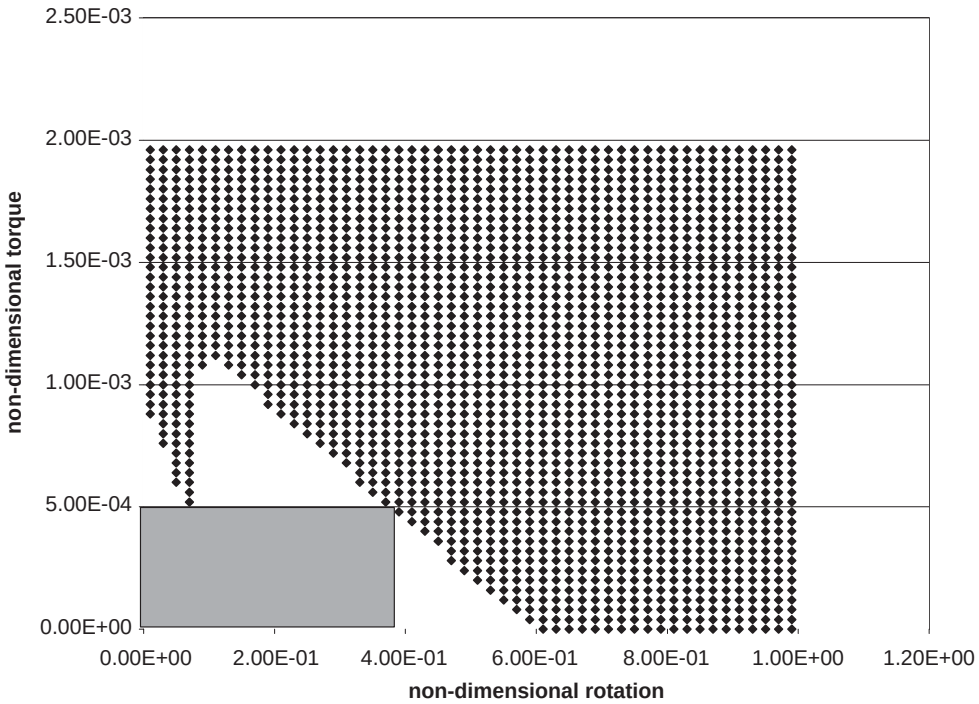

Fig. 20. Instabilities for the automotive model for $C_{iv} = 15.5\,\mathrm{N\,s/m}$.

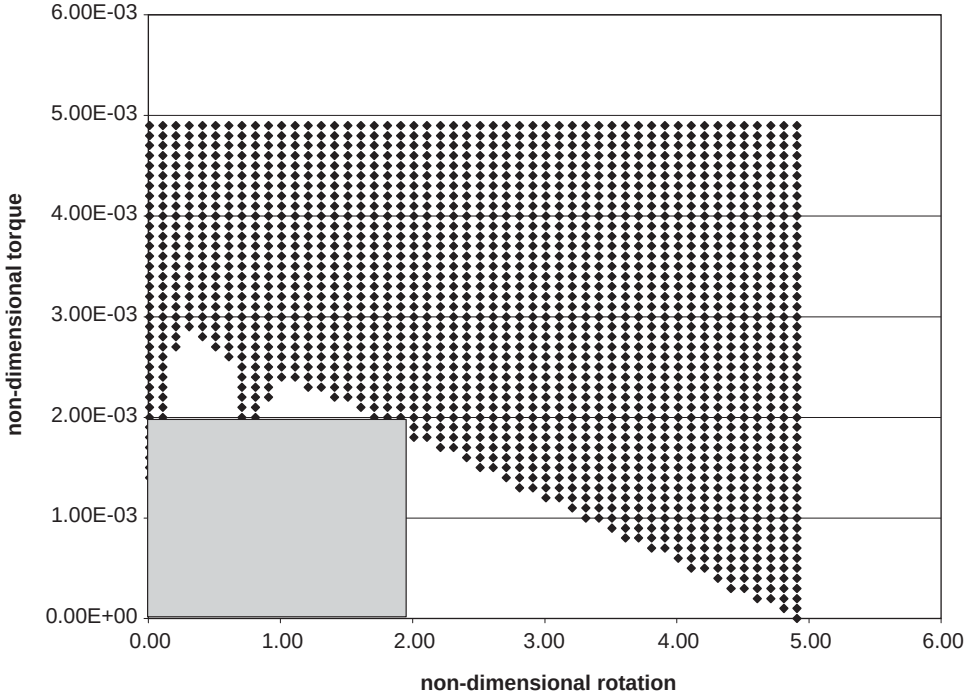

Fig. 21. Instabilities for the lab model for $C_{iv} = 0.042\,\mathrm{N\,s/m}$.

are outside the range of operation. Therefore, for the automotive example this value of internal damping (and all larger values) will lead to stable operational conditions in the entire range of operation.

Next the lab shaft is examined. Fig. 21 shows the instability zones for the shaft with a value of $C_{iv} = 0.042\,\mathrm{N\,s/m}$. Note that some parametric instabilities are found inside the range of operation (and so will also occur for the other values given in Table 2). For the lab case it is not possible to completely rid the system of instabilities through increase of internal damping.

6. Conclusions

Increasing internal damping is always stabilizing as regards to parametric instabilities.

For flutter instabilities the situation is more complex. Increasing internal damping is always stabilizing for rotational speeds below the first critical speed, v_1. For $v > v_1$, there is a value of C_{iv}, which depends on v and Γ_1, above which destabilization occurs.

The values of C_{iv} at which the flutter unstable zone first enters the practical range were determined as a function of external damping. For the automotive shaft it was found that a four-fold increase in external damping led to an increase of about 20% of the critical value. It was found that these values of C_{iv} also removed parametric instabilities out of the practical range.

For the lab model an increase in external damping of two orders of magnitude led to a change in the critical value of only about 10%. The lab model showed that it is not always possible to completely stabilize the system by increasing the internal damping. On using C_{iv} critical, parametric instabilities are still found in the practical range of operation.

Appendix A. Galerkin coefficients

$$\int_0^1 \frac{\mathrm{d}^4\Phi_m}{\mathrm{d}Z^4}(Z)\Phi_i(Z)\,\mathrm{d}Z = \alpha_{1_{mi}}, \quad \int_0^1 \frac{\mathrm{d}^4\Psi_m}{\mathrm{d}Z^4}(Z)\Psi_i(Z)\,\mathrm{d}Z = \alpha_{2_{mi}}, \quad \int_0^1 \Phi_m(Z)\Phi_i(Z)\,\mathrm{d}Z = \gamma_{1_{mi}},$$

$$\int_0^1 \Psi_m(Z)\Psi_i(Z)\,\mathrm{d}Z = \gamma_{2_{mi}}, \quad \int_0^1 \Psi_i(Z)\Phi_m(Z)\,\mathrm{d}Z = \gamma_{3_{mi}}, \quad \int_0^1 \Phi_i(Z)\Psi_m(Z)\,\mathrm{d}Z = \gamma_{4_{mi}},$$

$$\int_0^1 \Phi_m(Z)|_{Z=1}\Phi_i(Z)\Lambda(Z-1)\,\mathrm{d}Z = \Phi_m(Z)|_{Z=1}\Phi_i(Z)|_{Z=1} = \xi_{1_{mi}},$$

$$\int_0^1 \Psi_m(Z)|_{Z=1}\Psi_i(Z)\Lambda(Z-1)\,\mathrm{d}Z = \Psi_m(Z)|_{Z=1}\Psi_i(Z)|_{Z=1} = \xi_{2_{mi}},$$

$$\int_0^1 \left.\frac{\mathrm{d}\Psi_m(Z)}{\mathrm{d}Z}\right|_{z=0} \Phi_i(Z)\frac{\mathrm{d}\Lambda(Z)}{\mathrm{d}Z}\,\mathrm{d}Z = -\left.\frac{\mathrm{d}\Psi_m(Z)}{\mathrm{d}Z}\right|_{z=0} \left.\frac{\mathrm{d}\Phi_i(Z)}{\mathrm{d}Z}\right|_{z=0} = -2\delta_{3_{mi}},$$

$$\int_0^1 \left.\frac{\mathrm{d}\Phi_m(Z)}{\mathrm{d}Z}\right|_{z=0} \Psi_i(Z)\frac{\mathrm{d}\Lambda(Z)}{\mathrm{d}Z}\,\mathrm{d}Z = -\left.\frac{\mathrm{d}\Phi_m(Z)}{\mathrm{d}Z}\right|_{z=0} \left.\frac{\mathrm{d}\Psi_i(Z)}{\mathrm{d}Z}\right|_{z=0} = -2\delta_{2_{mi}},$$

$$\int_0^1 \left.\frac{\mathrm{d}\Phi_m(Z)}{\mathrm{d}Z}\right|_{z=0} \Phi_i(Z)\frac{\mathrm{d}\Lambda(Z)}{\mathrm{d}Z}\,\mathrm{d}Z = -\left.\frac{\mathrm{d}\Phi_m(Z)}{\mathrm{d}Z}\right|_{z=0} \left.\frac{\mathrm{d}\Phi_i(Z)}{\mathrm{d}Z}\right|_{z=0} = -2\delta_{1_{mi}},$$

$$\int_0^1 \left.\frac{\mathrm{d}\Psi_m(Z)}{\mathrm{d}Z}\right|_{z=0} \Psi_i(Z)\frac{\mathrm{d}\Lambda(Z)}{\mathrm{d}Z}\,\mathrm{d}Z = -\left.\frac{\mathrm{d}\Psi_m(Z)}{\mathrm{d}Z}\right|_{z=0} \left.\frac{\mathrm{d}\Psi_i(Z)}{\mathrm{d}Z}\right|_{z=0} = -2\delta_{4_{mi}},$$

$$\int_0^1 \frac{\mathrm{d}^3\Psi_m}{\mathrm{d}Z^3}(Z)\Phi_i(Z)\,\mathrm{d}Z = \beta_{1_{mi}}, \quad \int_0^1 \frac{\mathrm{d}^3\Phi_m}{\mathrm{d}Z^3}(Z)\Psi_i(Z)\,\mathrm{d}Z = \beta_{2_{mi}},$$

$$\int_0^1 \frac{\mathrm{d}^2\Phi_m}{\mathrm{d}Z^2}(Z)\Phi_i(Z)\,\mathrm{d}Z = \lambda_{1_{mi}}, \quad \int_0^1 \frac{\mathrm{d}^2\Psi_m}{\mathrm{d}Z^2}(Z)\Psi_i(Z)\,\mathrm{d}Z = \lambda_{2_{mi}},$$

$$\int_0^1 \frac{\mathrm{d}^2\Psi_m}{\mathrm{d}Z^2}(Z)\Phi_i(Z)\,\mathrm{d}Z = \lambda_{3_{mi}}, \quad \int_0^1 \frac{\mathrm{d}^2\Phi_m}{\mathrm{d}Z^2}(Z)\Psi_i(Z)\,\mathrm{d}Z = \lambda_{4_{mi}},$$

$$\int_0^1 \Phi_m(Z)\frac{\mathrm{d}\Lambda(Z)}{\mathrm{d}Z}\,\mathrm{d}Z = -\Phi'_m(0), \quad \int_0^1 \Psi_m(Z)\frac{\mathrm{d}\Lambda(Z)}{\mathrm{d}Z}\,\mathrm{d}Z = -\Psi'_m(0).$$

The above integrals were evaluated numerically using MAPLE. The following properties of the Dirac delta function were also used in deriving some of the above results:

$$\int_a^b \Delta(Z-\varsigma)g(Z)\,\mathrm{d}Z = g(\varsigma), \quad \int_a^b \frac{\mathrm{d}\Delta(Z-\varsigma)}{\mathrm{d}Z} g(Z)\,\mathrm{d}Z = -\left.\frac{\mathrm{d}g(Z)}{\mathrm{d}Z}\right|_{Z=\varsigma}, \quad a<\varsigma<b.$$

References

[1] A.J. Mazzei Jr., A. Argento, R.A. Scott, Dynamic stability of a rotating shaft driven through a universal joint, Journal of Sound and Vibration 222 (1) (1999) 19–47.

[2] A. Tondl, Some Problems of Rotor Dynamics, Chapman & Hall, London, 1965.

[3] J. Melanson, J.W. Zu, Free vibration and stability analysis of internally damped rotating shafts with general boundary conditions, Journal of Vibration and Acoustics 120 (1998) 776–783.

[4] F.F. Ehrich, Shaft whirl induced by rotor internal damping, Journal of Applied Mechanics 31 (1964) 279–282.

[5] W. Kliem, C. Pommer, J. Stoustrup, Stability of rotor systems: a complex modeling approach, Zeitschrift fuer Angewandte Mathematik Physik 49 (1998) 644–655.

[6] A.D. Dimarogonas, S. Haddad, Vibration for Engineers, Prentice Hall, Englewood Cliffs, NJ, 1992.

[7] W. Kim, A. Argento, R.A. Scott, Forced vibration and dynamic stability of a rotating tapered composite shaft: bending motions in end-milling operations, Journal of Sound and Vibration 246 (2001) 583–600.

[8] T. Iwatsubo, Stability problems on rotor systems, The Shock and Vibration Digest 11 (3) (1979) 17–26.

[9] L. Meirovich, Methods of Analytical Dynamics, McGraw-Hill Book Company, New York, 1970.